DNA Repair 10 (2011) 314–321

Contents lists available at ScienceDirect

DNA Repair

journal homepage: www.elsevier.com/locate/dnarepair

Two unrelated patients with *MRE11A* mutations and Nijmegen breakage syndrome-like severe microcephaly

Yoshiyuki Matsumoto[a], Tatsuo Miyamoto[a], Hiromi Sakamoto[a], Hideki Izumi[a], Yuka Nakazawa[b], Tomoo Ogi[b], Hidetoshi Tahara[c], Shozo Oku[d], Azuma Hiramoto[e], Toshihide Shiiki[f], Yoshiki Fujisawa[g], Hirofumi Ohashi[h], Yoshihiro Sakemi[i], Shinya Matsuura[a,*]

[a] *Department of Genetics and Cell Biology, Research Institute for Radiation Biology and Medicine, Hiroshima University, Kasumi 1-2-3, Minami-ku, Hiroshima 734-8553, Japan*
[b] *Department of Molecular Medicine, Atomic Bomb Disease Institute, Nagasaki University, Sakamoto 1-12-4, Nagasaki 852-8523, Japan*
[c] *Department of Cellular and Molecular Biology, Graduate School of Biomedical Sciences, Hiroshima University, Kasumi 1-2-3, Minami-ku, Hiroshima 734-8553, Japan*
[d] *Kagoshima Kodomo Hospital, Ijuin-cho 2-2000-669, Hioki 899-2503, Japan*
[e] *Hokkaido Ryoikuen, Shunkoudai 4-10, Asahikawa 071-8144, Japan*
[f] *Tobu Ryoiku Center, Shinsuna 3-3-25, Koutou-ku 136-0075, Tokyo, Japan*
[g] *Ehime Prefectural Central Hospital, Kasugamachi 83, Matsuyama 790-0024, Japan*
[h] *Saitama Children's Medical Center, Iwatsuki-ku, Saitama 339-8551, Japan*
[i] *Beppu Medical Center, Uchikamado, Beppu 874-0011, Japan*

ARTICLE INFO

Article history:
Received 19 August 2010
Received in revised form
25 November 2010
Accepted 10 December 2010
Available online 12 January 2011

Keywords:
Nijmegen breakage syndrome (NBS)
Ataxia–telangiectasia-like disorder (ATLD)
Nijmegen breakage syndrome-like disorder (NBSLD)
ATM
MRE11
NBS1
Microcephaly

ABSTRACT

MRE11 and NBS1 function together as components of a MRE11/RAD50/NBS1 protein complex, however deficiency of either protein does not result in the same clinical features. Mutations in the *NBN* gene underlie Nijmegen breakage syndrome (NBS), a chromosomal instability syndrome characterized by microcephaly, bird-like faces, growth and mental retardation, and cellular radiosensitivity. Additionally, mutations in the *MRE11A* gene are known to lead to an ataxia–telangiectasia-like disorder (ATLD), a late-onset, slowly progressive variant of ataxia–telangiectasia without microcephaly. Here we describe two unrelated patients with NBS-like severe microcephaly (head circumference −10.2 SD and −12.8 SD) and mutations in the *MRE11A* gene. Both patients were compound heterozygotes for a truncating or missense mutation and carried a translationally silent mutation. The truncating and missense mutations were assumed to be functionally debilitating. The translationally silent mutation common to both patients had an effect on splicing efficiency resulting in reduced but normal MRE11 protein. Their levels of radiation-induced activation of ATM were higher than those in ATLD cells.

1. Introduction

The development of the central nervous system is highly sensitive to DNA damaging agents and therefore several autosomal recessive disorders with defective DNA damage repair exhibit neurological abnormalities such as microcephaly and neurodegeneration [1,2].

The MRE11/RAD50/NBS1 (MRN) protein complex and the ataxia–telangiectasia mutated (ATM) protein, together play a central role in DNA double strand break repair [3]. Mutations in the *ATM* (MIM# 607585) and *MRE11A* (MIM# 600814) genes each give rise to a progressive cerebellar ataxia syndrome: *ATM* mutations to ataxia–telangiectasia (A–T [MIM# 208900]) [4], and *MRE11A* mutations to ataxia–telangiectasia-like disorder (ATLD [MIM# 604391]) [5,6]. A–T is an autosomal recessive disorder characterized by growth deficiency, progressive cerebellar ataxia, dysarthria, telangiectasia, frequent respiratory infections, and immunodeficiency. ATLD is also characterized by cerebellar ataxia, but its onset is later in life and its progression is slower than in A–T. In addition, there is no telangiectasia and immunoglobulin levels are normal.

Mutations in two different genes involved in the MRE11/RAD50/NBS1 complex are known to lead to a hereditary disorder with severe microcephaly: the *NBN* gene (MIM# 602667) to Nijmegen breakage syndrome (NBS [MIM# 251260]) [7–9], and the *RAD50* gene (MIM# 604040) to Nijmegen breakage syndrome-like disorder (NBSLD [MIM# 613078]) [10]. NBS is an autosomal recessive disorder characterized by microcephaly, growth and mental retardation, immunodeficiency, radiosensitivity, and cancer predisposition; NBSLD is a disorder with microcephaly, mental retardation, bird-like face, and short stature,

* Corresponding author. Tel.: +81 82 257 5809; fax: +81 82 256 7101.
E-mail address: shinya@hiroshima-u.ac.jp (S. Matsuura).

1568-7864/$ – see front matter © 2010 Elsevier B.V. All rights reserved.
doi:10.1016/j.dnarep.2010.12.002

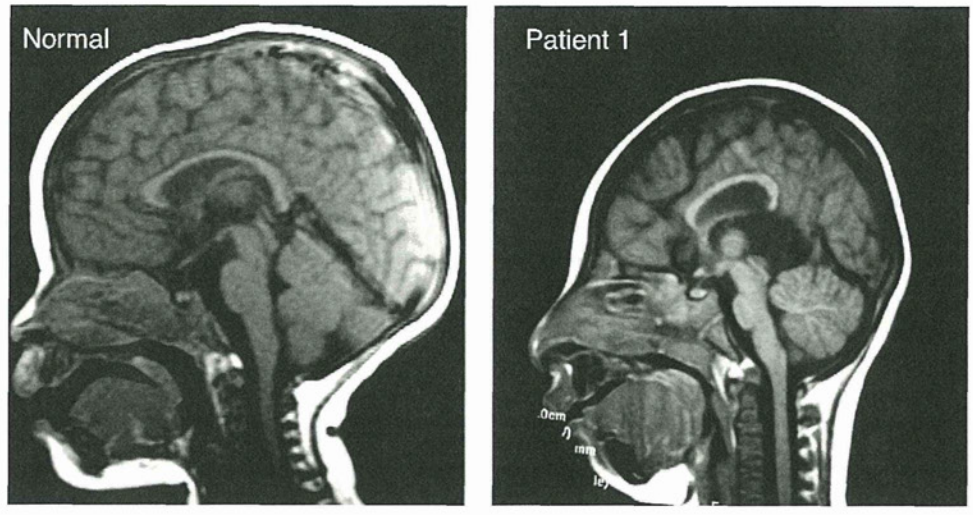

Fig. 1. Sagittal brain magnetic resonance imaging. (Left) Normal individual. (Right) Patient 1 at age 18 months with generalized cerebral hypodysplasia.

but without severe infections, immunodeficiency, or cancer predisposition.

We here describe two unrelated patients with Nijmegen breakage syndrome-like severe microcephaly and compound heterozygous mutations in the *MRE11A* gene.

2. Materials and methods

2.1. Clinical report

A 35-year-old woman was referred to us at 18 weeks of pregnancy for evaluation of intrauterine growth retardation. Ultrasound scan showed a fetus with a small femora and a disproportionately small head. Caesarian section was performed at 32 weeks of pregnancy, and a boy (Patient 1), was delivered. His birth weight was 966 g (−4.8 SD), length 35 cm (−6.7 SD), and head circumference 22 cm (−8.1 SD). He had severe microcephaly, a bird-headed facial appearance with receding forehead, and a prominent nose. Anterior fontanel was not palpable. His parents and two elder brothers were all healthy and phenotypically normal. There was no family history of consanguinity. Brain magnetic resonance imaging at age 18 months demonstrated hypoplasia of the cerebrum, smooth gyri, and enlarged lateral ventricles (Fig. 1). He had patent ductus arteriosus, which was surgically corrected at age 5 months. Bilateral cryptochidism was operated on at age 3 years. He stood holding onto a chair at age 30 months, sat alone with a stoop at age 3 years, and walked at age 3 years. At age 3.5 years, he weighed 7.4 kg (−4.1 SD), measured 78.5 cm (−4.8 SD), and had a head circumference of 34 cm (−10.2 SD). G-banded chromosomes were 46, XY. He had no severe or recurrent infections and his immunoglobulin levels were normal. Now aged 8 years, he is toilet trained, speaks several meaningful words, but does not speak a two-word-sentence. He attends a primary school, and is affable and friendly. He is farsighted with astigmatism. He is able to run with a slow pitch and kick a soccer ball. He shows neither ocular apraxia nor cerebellar ataxia.

Patient 2, a boy, was born at 37 weeks of gestation to a 29-year-old mother and a 28-year-old father, both healthy and unrelated. The pregnancy was unremarkable. An older brother was healthy without malformations. Birth weight was 1560 g (−4.1 SD), length 39 cm (−5.9 SD), and head circumference 25 cm (−6.1 SD). At age 30 months, he sat alone but could not stand or walk. At age 5 years, he shuffled while sitting, but was unable to stand. At age 13 years, he weighed 9.2 kg (−4.2 SD), measured 97 cm (−7.0 SD), and had a head circumference of 35 cm (−12.8 SD). He had severe microcephaly, a bird-like face with sloping forehead, a big nose, large and simple ears, short palpebral fissures, a small mouth, and a small and receding chin. His shoulders, elbows, hips, and knees exhibited a decreased range of motion. Also noted were scoliosis, subluxation of the left elbow joint, bilateral cryptorchidism, and bilateral talipes equinus. His tendon reflexes were slightly exaggerated. G-banded chromosomes were 46, XY. His immunoglobulin levels were normal. Now aged 33, he lives in an institution for handicapped individuals. He does not speak meaningful words, but recognizes people, communicates by gesture, and shows fondness by touching. He is bedridden, is unable to roll over, and is handfed. He did not develop secondary sexual characteristics. He does not show ocular apraxia and had neither malignancy nor severe infections.

2.2. Immortalized skin fibroblast cells

Informed consent was obtained from Patients 1 and 2 and their families prior to this study. Primary skin fibroblast cells cultured from the two patients were immortalized by transfection with an SV40 virus and phTERT retrovirus vector [11]. We used as references immortalized fibroblast cell lines (designated as SVT) from various related disorders: NBS (GM7166VA7) [12], A–T (AT5BIVA) [13], and ATLD (D6807-SVT) [6,14]. A fibroblast cell line from a normal individual (SM-SVT) served as a control. A mouse hybrid cell line A9(neo11)-1 containing human chromosome 11 was provided by Dr. M. Oshimura, and microcell-mediated chromosome transfer was performed as previously described [12]. Fibroblast cell lines were maintained in D-MEM supplemented with 10% fetal bovine serum (Hyclone, Logan, UT, USA).

2.3. EB virus-transformed lymphoblastoid cell lines (LCLs)

LCLs were established from peripheral blood lymphocytes of the two patients and their family members. We used LCLs from NBS (94P247) [9], ATLD (200704L), and A–T as references, and a LCL from a normal individual (96-007M) as a control. A NBS cell line (94P247) was provided by Dr. K. Sperling. An ATLD cell line (200704L) was established from a blood sample from a boy with ATLD [15], supplied by Drs. S. Nonoyama and K. Imai. LCLs were cultured in RPMI 1640 with 20% fetal bovine serum.

2.4. Mutational analysis

PCR primers for *MRE11A* gene (GenBank NM_005591.3) were synthesized to amplify all coding exons and intron–exon boundaries [16]. PCR products were directly sequenced using an ABI

PRISM 3130 Genetic Analyzer (Applied Biosystems, Foster City, CA). RT-PCR primers were synthesized to amplify the *MRE11A* cDNA spanning exons 1–8 (5′-CGAAAAGAAGACAGCCTTGG-3′ and 5′-TCCAAAAATTGTTCTGGAATGA-3′) (GenBank NM_005590.3). RT-PCR products were visualized following electrophoresis on a 2% NuSieve agarose gel. PCR primers for *RAD50* (GenBank Z75311.1) and *NBN* cDNAs (GenBank AF058696.2) were synthesized to amplify the open reading frame with several overlapping segments.

Transcript levels of the *MRE11A*-c.338A and *MRE11A*-c.338G alleles in LCLs from a normal individual, Patient 2 and the parents were determined by the cycleave quantitative real time PCR assay (Cycleave-qPCR, TaKaRa Co. Ltd.) carried out in triplicate. Transcripts from the *HPRT1* allele were used as a quantification control. RNaseH sensitive fluorescent probes that specifically recognize the *MRE11A*-c.338A and *MRE11A*-c.338G alleles were used for the assay. The qPCR results were analyzed by the ΔΔCT method. qPCR primers and probes used for the assay are listed below.

MRE11A-F: 5′-ACGTTTGTAACACTCGATGAA-3′;
MRE11A-R: 5′-CTGGAATTGAAATGTTGAGG-3′;
MRE11Ac.338A: (Eclipse) 5′-dAdAdG(A)dTdGdGdCdAdA-3′ (FAM);
MRE11Ac.338G: (Eclipse) 5′-dAdAdG(G)dTdGdGdCdA-3′ (ROX);
HPRT1-F: 5′-CAGGCAGTATAATCCAAAGATG-3′;
HPRT1-R: 5′-ACTGGCGATGTCAATAGGA-3′;
HPRT1-probe: (Eclipse) 5′-dCdAdGdCdA(A)dGdCdT-3′ (FAM).

2.5. Western blot analysis

Western blotting was performed as described previously [17]. Primary antibodies used were: mouse anti-MRE11 monoclonal antibody (MRE11-12D7, 1:1000, GeneTex, Irvine, CA); mouse anti-RAD50 monoclonal antibody (13B3/2C6, 1:1000, GeneTex, Irvine, CA); rabbit anti-NBS1 polyclonal antibody (NB100-142, 1:500, Novus Biologicals, Littleton, CO); mouse anti-GAPDH monoclonal antibody (6C5, 1:1000, Santa Cruz Biotechnology, Santa Cruz, CA); and mouse anti-β-tubulin monoclonal antibody (1:2000, Sigma–Aldrich, St. Louis, MO).

2.6. Radiation-sensitivity analysis

Clonogenic analysis was performed on fibroblast cell lines to learn of their radiosensitivity as previously described [12]. Chromosome breakage analysis of LCLs was carried out as follows. Cells were irradiated with 2 Gy X-ray and harvested 24 h after irradiation. Giemsa-stained chromosome slides were prepared, and chromatid or chromosome breaks and quadriradials were counted.

2.7. ATM autophosphorylation after γ-irradiation

Immortalized fibroblast cells or LCLs were irradiated with 0.5 Gy of γ ray. At 15 min and 30 min after irradiation, the cells were analyzed with Western blotting using rabbit anti-ATM-p1981 monoclonal antibody (1:1000, Epitomics Inc., Burlingame, CA) and mouse anti-ATM monoclonal antibody (2C1, 1:1000, GeneTex, Irvine, CA). Band intensities were estimated using a densitometer and are presented as means ± standard deviation. The statistical differences were analyzed with Student's *t*-test. Statistical significance was assumed for $p < 0.05$.

2.8. DNA damage response assay

ATM-dependent G2/M checkpoint arrest was performed according to the methods described previously [18].

2.9. p53 phosphorylation after γ-irradiation

Lymphoblastoid cells were irradiated with 0.5 Gy of γ ray. At 15 min and 30 min after irradiation, the cells were analyzed with Western blotting using rabbit anti-phosphorylated p53 (Ser15) polyclonal antibody (1:1000, Cell Signaling Technology, Beverly, MA) and mouse anti-p53 monoclonal antibody (1:1000, Oncogene Research Products, CA).

2.10. Caspase 3 activation after γ-irradiation

Immortalized fibroblast cells were irradiated with 0 or 10 Gy of γ ray. At 72 h after irradiation the cells were analyzed with Western blotting using rabbit anti-cleaved caspase 3 monoclonal antibody (#9664, 1:1000, Cell Signaling Technology, Beverly, MA).

3. Results

3.1. Identification of MRE11A mutations

Several studies have demonstrated that microcephaly, as was present in the two patients we described, is a common feature in a variety of DNA damage repair defective disorders [2]. Therefore, we examined DNA damage repair proteins including ATM, ATR, MRE11, RAD50, and NBS1 in the two patients. Western blot analysis showed normal levels of ATM and ATR (data not shown) and reduced levels of MRE11, RAD50, and NBS1 in both patients (Fig. 2a). We, therefore, sequenced all the *MRE11A*, *RAD50*, and *NBN* coding sequences in both patients and found only the *MRE11A* mutations c.658A>C and c.659+1G>A in Patient 1, and c.658A>C and c.338A>G in Patient 2 (Fig. 2b). In Patient 1, c.658A>C was derived from the father, and c.659+1G>A from the mother. Two brothers were a heterozygote for c.659+1G>A. RT-PCR and sequencing analysis demonstrated that c.659+1G>A resulted in exon 7 skipping leading to a premature termination codon (p.Ser183ValfsX31) (Fig. 2c). The c.658A>C substitution located within exon 7 did not alter amino acids but affected splicing efficiency that resulted in exon 7 skipping (Fig. 2c). RT-PCR analysis of exons 1–8 of *MRE11A* cDNA from Patient 1 detected a reduced but considerable amount of correctly spliced transcripts in addition to the exon-skipped transcript (Fig. 2c). Western blot analysis of fibroblasts from Patient 1 detected a reduced amount of normal-sized MRE11 protein (Fig. 2a). No smaller-sized protein corresponding to the predicted truncated form was detected in both lymphocytes and fibroblasts. The c.658A>C substitution was not found in 100 normal Japanese individuals. These results indicated that the c.658A>C mutation leads to exon 7 skipping but that some of the RNA is correctly spliced.

Patient 2 was another compound heterozygote with c.658A>C, the same single-base substitution as the one found in Patient 1, and c.338A>G, a single-base substitution in exon 5. The c.658A>C substitution was inherited from the mother while c.338A>G was derived from the father. A DNA sample from the older brother was not available. Cloning and sequencing of the RT-PCR products of Patient 2 revealed two kinds of mRNA from the c.338G allele; normal sized transcripts carrying the c.338A>G substitution and intermediately sized transcripts resulting from exon 5 skipping (Fig. 2c). The normal sized products lead to an amino acid substitution of Asp to Gly at the 113th residue (p.Asp113Gly). The 113th residue is located within the highly conserved phosphoesterase domain, which is essential for endonuclease activity [19]. On the other hand, the intermediately sized transcripts resulting from exon 5 skipping lead to a premature termination codon (p.Phe106GlnfsX10). We then examined the levels of the transcripts from the c.338A and c.338G alleles by quantitative RT-PCR analysis. The correctly spliced

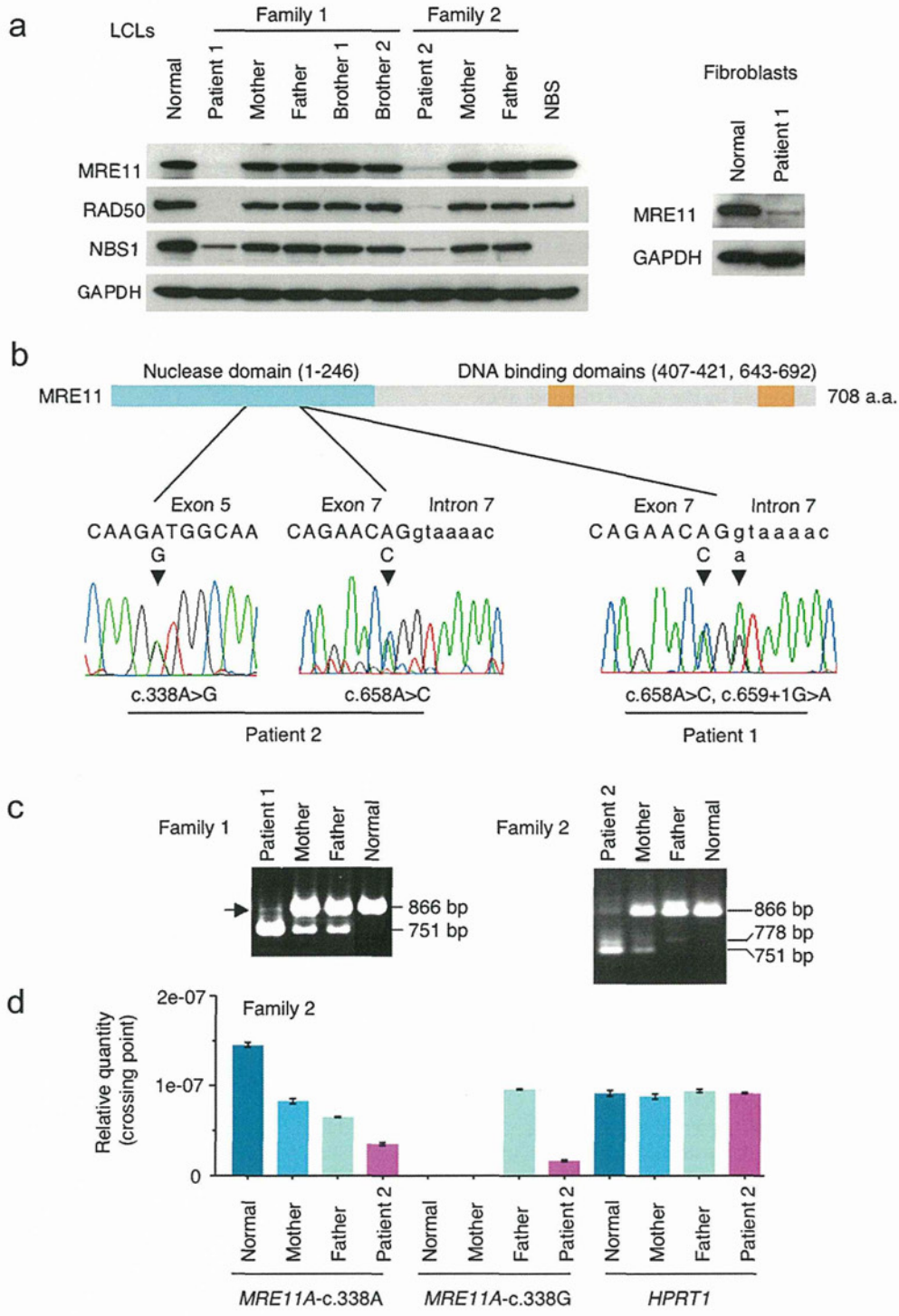

Fig. 2. MRE11 deficiencies associated with *MRE11A* mutations. (a) Western blot analyses of MRE11, RAD50, and NBS1 in lymphoblastoid cell lines (LCLs) from Patients 1 and 2 and their family members. Nijmegen breakage syndrome (NBS) cells were used as an NBS1-deficient reference, and anti-GAPDH antibody for equal loading. Levels of MRE11, RAD50, and NBS1 were reduced in both patients. Right panel shows a reduced MRE11 protein band of normal size in fibroblasts from Patient 1. (b) MRE11 protein structure and *MRE11A* mutations in Patients 1 and 2 as determined by genomic DNA sequencing. Patient 1 was a compound heterozygote with c.658A>C, a single-base substitution in exon 7, and c.659+1G>A, a substitution at an exon–intron junction of the splice donor-site. Patient 2 was a compound heterozygote with c.658A>C, the same single-base substitution in exon 7, and c.338A>G, a single-base substitution in exon 5. (c) RT-PCR analyses of exons 1–8 of *MRE11A* cDNAs from Patients 1 and 2 and their family members. RT-PCR of Patient 1 yielded two bands of 866 bp and 751 bp. The 866 bp band corresponds to the correctly spliced transcripts, and the 751 bp band to exon 7-skipped transcripts. The arrow on the left margin indicates the transcripts from the c.658A>C mutant allele. Analyses in the parents yielded two bands of 866 bp and 751 bp. RT-PCR of Patient 2 showed three bands of 866 bp, 778 bp, and 751 bp. The 866 bp band corresponds to the correctly spliced transcripts from the c.658A>C allele and the c.338A>G allele. The 778 bp band corresponds to exon 5-skipped transcripts, and the 751 bp band to the exon 7-skipped transcripts. (d) Quantitative RT-PCR analysis of the transcript levels from the c.338A and the c.338G alleles of Patient 2 and their family members. Transcripts from the *HPRT1* allele were used as a quantification control. The correctly spliced transcripts from the c.338G allele of Patient 2 showed 25% of the normal level. By contrast, the transcript levels from the c.338G allele of the father were not affected.

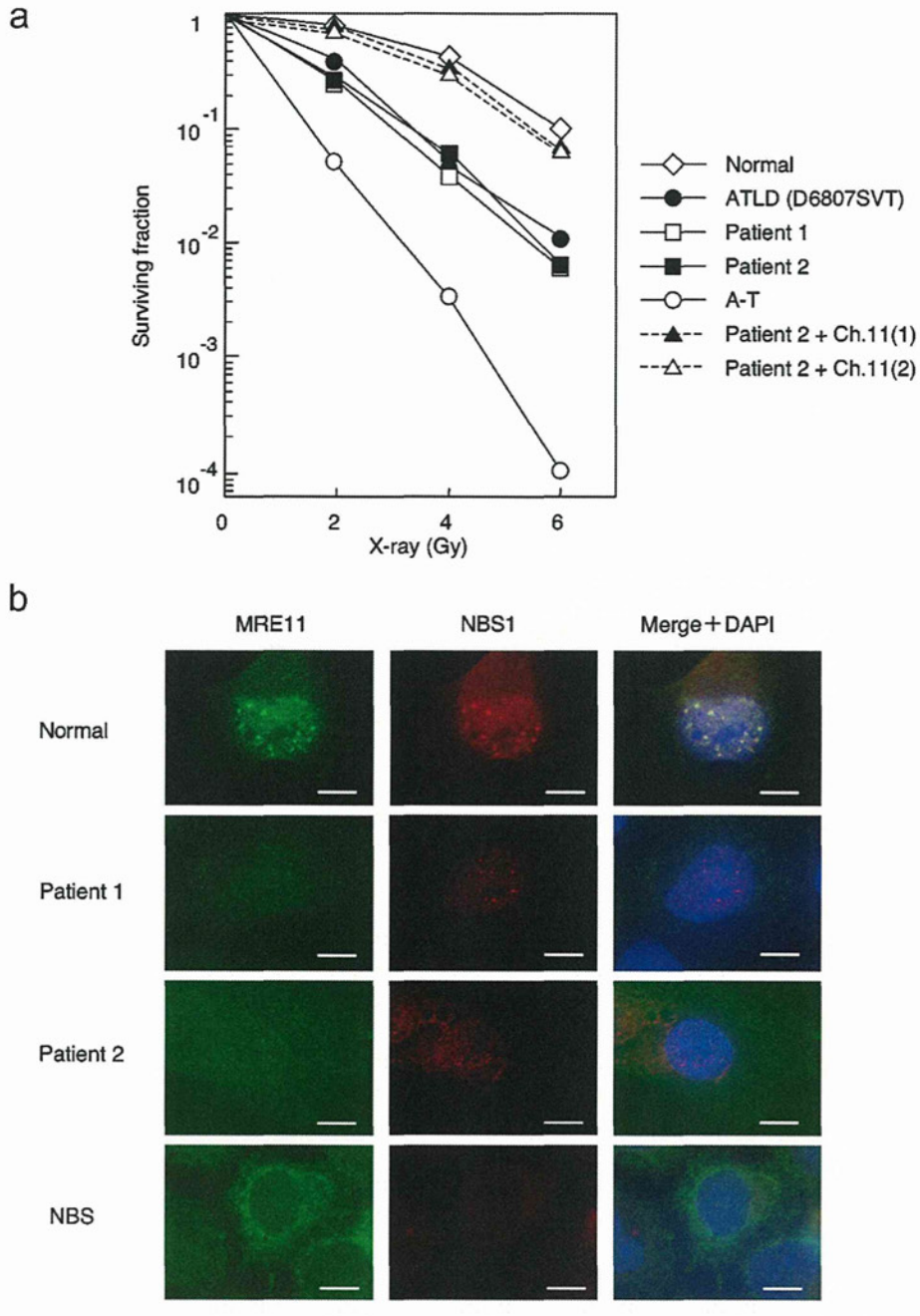

Fig. 3. Clonogenic survival curves for X-ray-irradiated fibroblasts. (a) Radiosensitivity was measured by counting colonies surviving radiation doses of 0–6 Gy. Colony survival was expressed as a logarithm. ATLD, ataxia–telangiectasia-like disorder; A–T, ataxia–telangiectasia. A–T cells were highly sensitive to radiation. Cells from Patients 1 and 2, and ATLD all showed intermediate levels of sensitivity. Microcell-mediated transfer of a human chromosome 11 (including the *MRE11A* locus) into the cells from Patient 2 restored radiation sensitivity. (b) Formation of MRE11 and NBS1 radiation-induced nuclear foci. Cells were analyzed by immuno-staining at 24 h after 6 Gy irradiation. Normal cells served as a control, and NBS cells served as an *NBN*-deficient reference. MRE11 and NBS1 formed nuclear foci after irradiation in normal cells. In contrast, cells from Patients 1 and 2 showed only very faint signals.

transcripts from the c.338G allele of Patient 2 showed 25% of the normal level (Fig. 2d). By contrast, the transcript levels from the c.338G allele of the father were not affected. The c.338A>G substitution was not detected in 100 normal Japanese individuals.

3.2. Cells from Patients 1 and 2 exhibit radiation-hypersensitivity

A clonogenic radiation sensitivity assay was performed on fibroblast cells from Patients 1 and 2 on ATLD and A–T cells as references, and on normal cells as a control. The cells from Patients 1 and 2, and ATLD were hypersensitive to X-ray irradiation, as measured by the share of surviving fractions after irradiation (Fig. 3a). A–T cells showed more marked radiation-hypersensitivity than in Patients 1 and 2, and ATLD. We introduced chromosome 11 (containing the *MRE11A* locus) into the cells from Patient 2 through microcell-mediated transfer [12]. Two microcell-hybrid clones obtained and both showed restoration of radiation-sensitivity (Fig. 3a).

Next, we studied MRE11 and NBS1 radiation-induced nuclear foci formation 24 h after exposure to 6 Gy. MRE11 and NBS1 formed nuclear foci after irradiation in normal cells. In contrast, cells from Patients 1 and 2 showed only very faint signals of NBS1 and MRE11. It is noteworthy that a few NBS1 foci were present in Patient 1. These findings are likely to be compatible with the level of the protein in the cells (Fig. 3b).

Table 1
Chromosomal aberrations in lymphocytes after 2 Gy irradiation.

Cells	No. of cells analyzed	Chromosome aberrations			Total no. of aberrations	Chromosome aberrations per cell
		Chromatid break	Chromosome break	Quadriradial chromosome		
Normal	100	10	17	3	20	0.20
ATLD	100	12	46	64	122	1.22
Patient 1	105	20	64	47	178	1.70
Patient 2	100	66	65	67	198	1.98
A–T	100	62	102	34	198	1.98

Table 1 lists chromosomal aberrations induced by ionizing radiation in LCLs from Patients 1 and 2, ATLD and A–T. Chromosome aberrations scored included chromatid and chromosome breaks and quadriradials. Cells from Patients 1 and 2 both showed an increase of aberrations comparable to those in ATLD and A–T cells.

3.3. Cells from Patients 1 and 2 have levels of ATM activation higher than those in ATLD cells

We analyzed cells from Patients 1 and 2, A–T, and ATLD for radiation-induced ATM activation. ATM is phosphorylated at serine residue 1981 in response to irradiation [20]. We therefore gave 0.5 Gy of γ ray radiation to LCLs from Patients 1 and 2, A–T, and ATLD, and analyzed with Western blotting the intensity of their phosphorylated ATM bands. The LCLs from Patients 1 and 2 showed an increased intensity of the phosphorylated ATM band after irradiation, while very little ATM phosphorylation was observed at 0 and 15 min after irradiation in ATLD cells (200704L), and a phosphorylated band appeared only after 30 min (Fig. 4a). The fibroblast cells of Patients 1 and 2, and ATLD (D6807SVT) showed responses similar to the LCLs (Fig. 4b).

3.4. Cells from Patients 1 and 2 have G2/M checkpoint defects, and levels of p53 and caspase 3 activation higher than those in ATLD cells

Mitotic index was examined in the cells irradiated with 2 Gy of γ ray in order to monitor the ATM-dependent G2/M checkpoint. Fibroblasts from Patients 1 and 2, and ATLD (D6807SVT) 30 min after irradiation all showed a slight decrease in mitotic index, intermediate between control and A–T cells. At 2 h after irradiation, cells from Patients 1 and 2 showed a decrease of mitotic index to the level of normal cells, while ATLD cells showed a response intermediate between the control and A–T cells (Fig. 5a).

We studied phosphorylation of p53, an ATM substrate, in the LCLs from Patients 1 and 2, A–T, and ATLD. The LCLs from Patients 1 and 2 showed an increase of p53 phosphorylation at serine residue 15 after irradiation, whereas ATLD cells showed a noticeably small increase of p53 phosphorylation (Fig. 5b). We also studied caspase 3 activation in the cells from Patients 1 and 2, A–T, and ATLD as an endpoint of ATM-dependent apoptosis by Western blotting. Caspase 3 cleavage was apparent after irradiation in normal cells and Patients 1 and 2 cells, but not in A–T and ATLD cells (Fig. 5c).

4. Discussion

We have described two unrelated patients with severe microcephaly resembling Nijmegen breakage syndrome (NBS). NBS is a hereditary disorder caused by biallelic mutations of the *NBN* gene [7–9]. It is characterized by severe microcephaly, a bird-like facial appearance, growth and mental retardation, chromosomal instability, and cellular radiosensitivity [21]. The two patients we described both had all these features, but they showed neither immunodeficiency nor cancer predisposition, as is typical of NBS. We sequenced the *NBN*, *MRE11A*, and *RAD50* coding sequences in both patients, and found only the *MRE11A* mutations. Patient 1 had c.658A>C substitution plus a splicing mutation in the *MRE11A* gene, and Patient 2 had c.658A>C substitution and c.338A>G substitution. The c.658A>C substitution common to both patients resulted in a reduced level of normally functioning MRE11 protein. On the other hand, the c.338A>G substitution in Patient 2 resulted in a reduced level of MRE11 protein with a single amino acid substitution in the highly conserved domain. Therefore, the splicing mutation in

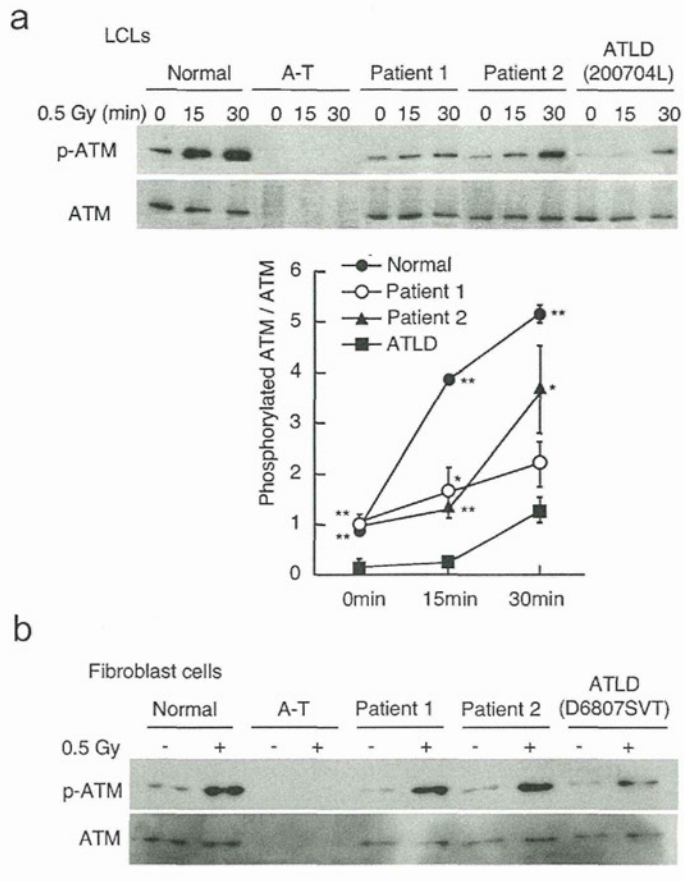

Fig. 4. Radiation-induced ATM activation. (a) Western blot analysis of phosphorylated ATM protein after irradiation of LCLs with 0.5 Gy γ ray. A–T cells served as an ATM-deficient cell line, and ATLD LCL (200704L) was used as a control. Phosphorylated ATM in LCLs from both Patients 1 and 2 increased after irradiation, while ATLD cells did not. ATLD LCL (200704L) was derived from a compound heterozygote for a *MRE11A* missense mutation (p.Trp243Arg) and a splicing mutation that resulted in exon 10 skipping, leading to an in-frame deletion (p.340–366del27) without correctly spliced transcripts [15]. The statistical significance of the differences in phosphorylated ATM/total ATM was examined by *t*-test. $^{*}p < 0.05$; $^{**}p < 0.01$ (normal, Patient 1, or Patient 2 versus ATLD). The data are shown as average ± standard error determined from three separate experiments. (b) Western blots of phospohrylated ATM protein at 30 min after irradiation of fibroblasts with 0.5 Gy of γ ray. A–T cells served as an ATM-deficient cell line, and ATLD fibroblasts (D6807SVT) harboring homozygous nonsense mutations were used as a control. Phosphorylated ATM in fibroblasts from both Patients 1 and 2 increased after irradiation, whereas ATLD cells did not.

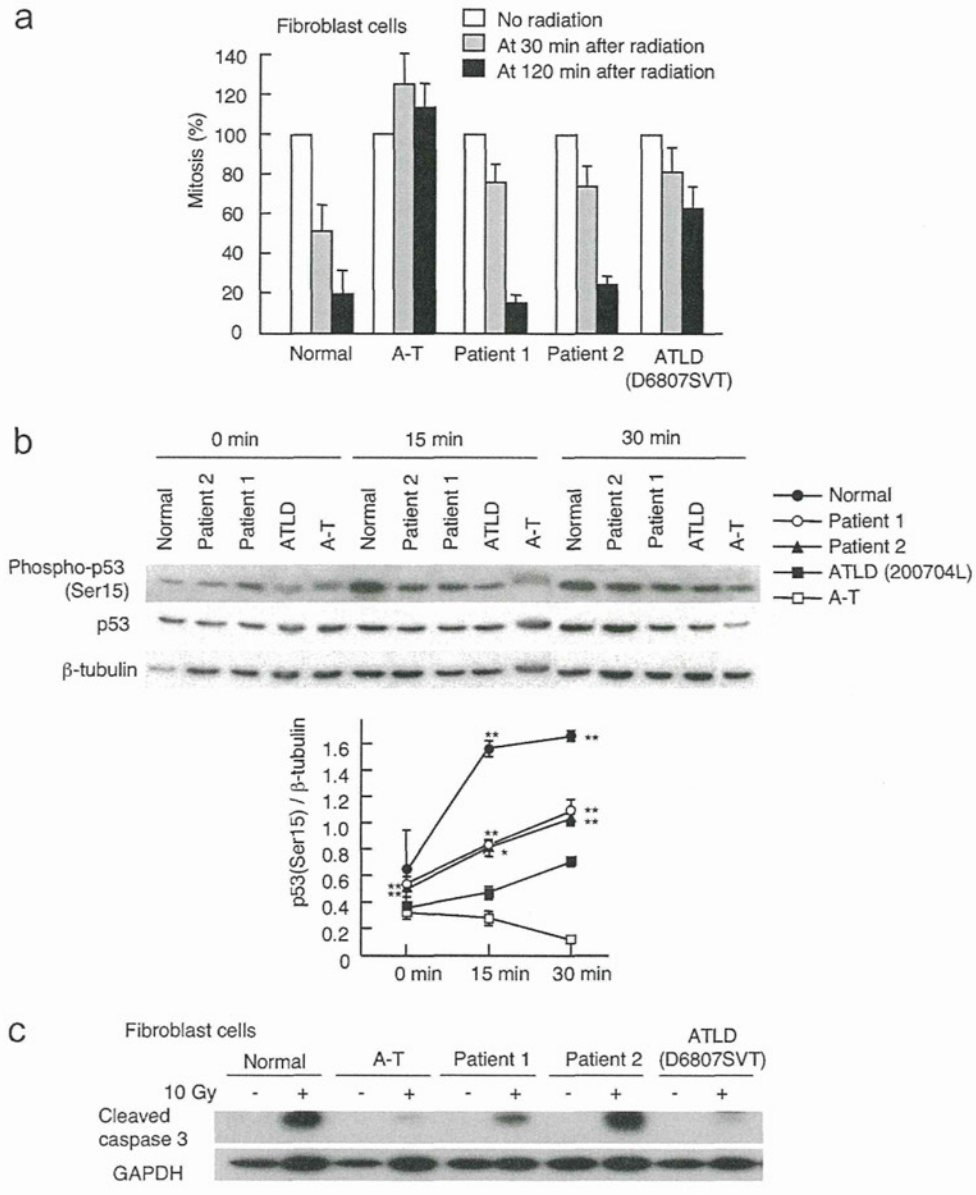

Fig. 5. Radiation-induced G2/M checkpoint and, p53 phosphorylation and caspase 3 activation as indicators of ATM activation deficiency. (a) Ataxia–telangiectasia (A–T) fibroblasts were used as an ATM-deficient reference, and ATLD fibroblasts (D6807SVT) harboring homozygous nonsense mutations were used as a control. Cultured fibroblast cells on a slide were irradiated with 2 Gy of γ ray, and stained 30 min or 2 h later with DAPI and rabbit anti-phospho-histone H3 polyclonal antibody. Mitotic index in each cell line without irradiation was estimated as 100%. Fibroblasts from Patients 1 and 2, and ATLD cells all showed a slight decrease in mitotic index at 30 min after irradiation, intermediate between normal and A–T cells. At 2 h after irradiation, cells from Patients 1 and 2 showed a decrease of mitotic index to the level of the normal cells, while ATLD cells showed a response intermediate between normal and A–T cells. Each column represents an average ± standard error from three separate experiments. (b) Western blots of phospohrylated p53 protein after irradiation. A–T and ATLD cells were used as controls. LCLs were irradiated with 0.5 Gy of γ ray. At 15 min and 30 min after irradiation, the cells were analyzed with Western blotting using rabbit anti-phosphorylated p53 (Ser15) polyclonal antibody (1:1000, Cell Signaling Technology, Beverly, MA) and mouse anti-p53 monoclonal antibody (1:1000, Oncogene Research Products, CA). Phosphorylated p53 in LCLs from Patients 1 and 2 increased after irradiation, whereas such an increase was smaller in ATLD cells. The statistical significance of the differences in phosphorylated p53/β-tubulin was tested by *t*-test. $*p < 0.05$; $**p < 0.01$ (normal, Patient 1, or Patient 2 versus ATLD). The data are shown as average ± standard error determined from three separate experiments. (c) Western blot analysis of cleaved caspase 3 protein after 10 Gy γ-irradiation of fibroblast cells. Cleaved caspase 3 bands were seen in normal, Patients 1 and 2 cells, but not in A–T and ATLD cells.

Patient 1 and the missense mutation in Patient 2 were assumed to be functionally debilitating.

MRE11A is known as the gene underlying ataxia–telangiectasia-like disorder (ATLD), a milder and slowly progressive variant of A–T without microcephaly [5]. To date, seven families with ATLD patients have been reported: two in the U.K., one in Italy, three in Saudi Arabia, and one in Japan. These patients with *MRE11A* mutations included: compound heterozygotes with a splicing mutation plus a missense mutation; homozygotes for a missense mutation; compound heterozygotes with a missense mutation plus a nonsense mutation; and homozygotes for a nonsense mutation.

It was reported that the MRE11/RAD50/NBS1 protein complex is involved in radiation-induced ATM activation [14]. We therefore analyzed level of radiation-induced ATM activation in cells from Patients 1 and 2, and those from ATLD patients. Cells from Patients 1 and 2 showed the level of ATM activation higher than those in ATLD cells. The cells from Patients 1 and 2 both showed the levels of p53 phosphorylation and caspase-3 activation higher than those in ATLD cells. The differences are likely to be attributable to the presence of normally functioning MRE11 protein in Patients 1 and 2.

Several explanations are conceivable for the unusual clinical features in the two patients. First, ATM-dependent neuronal apop-

tosis has been proposed as a mechanism underlying microcephaly in DNA damage disorders [2,22–24]. According to this model, the two patients might have undergone extensive neuronal apoptosis during development due to the relatively higher level of ATM activation, and developed severe microcephaly, while ATLD patients cannot activate ATM, thereby failing to engage in apoptosis but presenting with neurodegeneration. The second possibility is that the effect of microcephaly might be mediated through NBS1. Since *MRE11A* mutations often affect the levels of NBS1 and RAD50, and NBS1 deficiency uniformly leads to microcephaly, the effect of these *MRE11A* mutations might be indirect and those that result in greater diminution in the levels of NBS1 might be more prone to microcephaly. The third possibility is that an additional gene(s) other than *MRE11A* might be involved in development of microcephaly. The molecular mechanism underlying neuropathology remains to be elucidated.

In conclusion, we have identified and characterized the two patients with *MRE11A* mutations but severe microcephaly. This report suggests that MRE11 deficiency has a wider spectrum of the clinical features than that has been thought.

Conflict of interest statement

There is no conflict of interest.

Acknowledgements

We thank the families for their cooperation in the study, Drs. S. Nonoyama and K. Imai for providing ATLD cells, Dr. K. Sperling for NBS cells, Dr. M. Oshimura for a mouse hybrid cell line, Drs. J. Kobayashi and T. Ishii for discussion, Dr. M. Kobayashi for providing clinical information, and Ms. Y. Tonouchi for assistance. We thank Dr. T. Kajii for critically reading the manuscript. This work was supported by Grants-in-Aid for Scientific Research from the Ministry of Education, Culture, Sports, Science and Technology.

References

[1] A. Kulkarni, D.M. Wilson 3rd, The involvement of DNA-damage and -repair defects in neurological dysfunction, Am. J. Hum. Genet. 82 (2008) 539–566.
[2] M. O'Driscoll, P.A. Jeggo, The role of the DNA damage response pathways in brain development and microcephaly: insight from human disorders, DNA Repair (Amst.) 7 (2008) 1039–1050.
[3] M.F. Lavin, ATM and the Mre11 complex combine to recognize and signal DNA double-strand breaks, Oncogene 26 (2007) 7749–7758.
[4] M.F. Lavin, Ataxia–telangiectasia: from a rare disorder to a paradigm for cell signalling and cancer, Nat. Rev. Mol. Cell Biol. 9 (2008) 759–769.
[5] A.M. Taylor, A. Groom, P.J. Byrd, Ataxia–telangiectasia-like disorder (ATLD) – its clinical presentation and molecular basis, DNA Repair (Amst.) 3 (2004) 1219–1225.
[6] G.S. Stewart, R.S. Maser, T. Stankovic, D.A. Bressan, M.I. Kaplan, N.G. Jaspers, A. Raams, P.J. Byrd, J.H. Petrini, A.M. Taylor, The DNA double-strand break repair gene hMRE11 is mutated in individuals with an ataxia–telangiectasia-like disorder, Cell 99 (1999) 577–587.
[7] S. Matsuura, H. Tauchi, A. Nakamura, N. Kondo, S. Sakamoto, S. Endo, D. Smeets, B. Solder, B.H. Belohradsky, V.M. Der Kaloustian, M. Oshimura, M. Isomura, Y. Nakamura, K. Komatsu, Positional cloning of the gene for Nijmegen breakage syndrome, Nat. Genet. 19 (1998) 179–181.
[8] J.P. Carney, R.S. Maser, H. Olivares, E.M. Davis, M. Le Beau, J.R. Yates 3rd, L. Hays, W.F. Morgan, J.H. Petrini, The hMre11/hRad50 protein complex and Nijmegen breakage syndrome: linkage of double-strand break repair to the cellular DNA damage response, Cell 93 (1998) 477–486.
[9] R. Varon, C. Vissinga, M. Platzer, K.M. Cerosaletti, K.H. Chrzanowska, K. Saar, G. Beckmann, E. Seemanova, P.R. Cooper, N.J. Nowak, M. Stumm, C.M. Weemaes, R.A. Gatti, R.K. Wilson, M. Digweed, A. Rosenthal, K. Sperling, P. Concannon, A. Reis, Nibrin, a novel DNA double-strand break repair protein, is mutated in Nijmegen breakage syndrome, Cell 93 (1998) 467–476.
[10] R. Waltes, R. Kalb, M. Gatei, A.W. Kijas, M. Stumm, A. Sobeck, B. Wieland, R. Varon, Y. Lerenthal, M.F. Lavin, D. Schindler, T. Dork, Human RAD50 deficiency in a Nijmegen breakage syndrome-like disorder, Am. J. Hum. Genet. 84 (2009) 605–616.
[11] S.A. Carney, H. Tahara, C.D. Swartz, J.I. Risinger, H. He, A.B. Moore, J.K. Haseman, J.C. Barrett, D. Dixon, Immortalization of human uterine leiomyoma and myometrial cell lines after induction of telomerase activity: molecular and phenotypic characteristics, Lab. Invest. 82 (2002) 719–728.
[12] S. Matsuura, C. Weemaes, D. Smeets, H. Takami, N. Kondo, S. Sakamoto, N. Yano, A. Nakamura, H. Tauchi, S. Endo, M. Oshimura, K. Komatsu, Genetic mapping using microcell-mediated chromosome transfer suggests a locus for Nijmegen breakage syndrome at chromosome 8q21–24, Am. J. Hum. Genet. 60 (1997) 1487–1494.
[13] K. Komatsu, S. Kodama, Y. Okumura, M. Koi, M. Oshimura, Restoration of radiation resistance in ataxia telangiectasia cells by the introduction of normal human chromosome 11, Mutat. Res. 235 (1990) 59–63.
[14] T. Uziel, Y. Lerenthal, L. Moyal, Y. Andegeko, L. Mittelman, Y. Shiloh, Requirement of the MRN complex for ATM activation by DNA damage, EMBO J. 22 (2003) 5612–5621.
[15] N. Uchisaka, N. Takahashi, M. Sato, A. Kikuchi, S. Mochizuki, K. Imai, S. Nonoyama, O. Ohara, F. Watanabe, S. Mizutani, R. Hanada, T. Morio, Two brothers with ataxia–telangiectasia-like disorder with lung adenocarcinoma, J. Pediatr. 155 (2009) 435–438.
[16] S.A. Pitts, H.S. Kullar, T. Stankovic, G.S. Stewart, J.I. Last, T. Bedenham, S.J. Armstrong, M. Piane, L. Chessa, A.M. Taylor, P.J. Byrd, hMRE11: genomic structure and a null mutation identified in a transcript protected from nonsense-mediated mRNA decay, Hum. Mol. Genet. 10 (2001) 1155–1162.
[17] J. Kobayashi, H. Tauchi, S. Sakamoto, A. Nakamura, K. Morishima, S. Matsuura, T. Kobayashi, K. Tamai, K. Tanimoto, K. Komatsu, NBS1 localizes to gamma-H2AX foci through interaction with the FHA/BRCT domain, Curr. Biol. 12 (2002) 1846–1851.
[18] E. Griffith, S. Walker, C.A. Martin, P. Vagnarelli, T. Stiff, B. Vernay, N. Al Sanna, A. Saggar, B. Hamel, W.C. Earnshaw, P.A. Jeggo, A.P. Jackson, M. O'Driscoll, Mutations in pericentrin cause Seckel syndrome with defective ATR-dependent DNA damage signaling, Nat. Genet. 40 (2008) 232–236.
[19] R.S. Williams, G. Moncalian, J.S. Williams, Y. Yamada, O. Limbo, D.S. Shin, L.M. Groocock, D. Cahill, C. Hitomi, G. Guenther, D. Moiani, J.P. Carney, P. Russell, J.A. Tainer, Mre11 dimers coordinate DNA end bridging and nuclease processing in double-strand-break repair, Cell 135 (2008) 97–109.
[20] C.J. Bakkenist, M.B. Kastan, DNA damage activates ATM through intermolecular autophosphorylation and dimer dissociation, Nature 421 (2003) 499–506.
[21] S. Matsuura, J. Kobayashi, H. Tauchi, K. Komatsu, Nijmegen breakage syndrome and DNA double strand break repair by NBS1 complex, Adv. Biophys. 38 (2004) 65–80.
[22] P.O. Frappart, W.M. Tong, I. Demuth, I. Radovanovic, Z. Herceg, A. Aguzzi, M. Digweed, Z.Q. Wang, An essential function for NBS1 in the prevention of ataxia and cerebellar defects, Nat. Med. 11 (2005) 538–544.
[23] C. Barlow, K. Treuner, DNA instability in the brain: survival of the 'fittest', Nat. Med. 11 (2005) 474–475.
[24] E.R. Shull, Y. Lee, H. Nakane, T.H. Stracker, J. Zhao, H.R. Russell, J.H. Petrini, P.J. McKinnon, Differential DNA damage signaling accounts for distinct neural apoptotic responses in ATLD and NBS, Genes Dev. 23 (2009) 171–180.

Chapter 6

Telomere G-Overhang Length Measurement Method 2: G-Tail Telomere HPA

Hidetoshi Tahara

Abstract

Both telomere length and telomere G-tail length are altered in human diseases such as cancer and age-related disease. While most methods for the measurement of G-tail and telomere length require electrophoresis, centrifugation, radioisotope labeling, and autoradiography, G-tail telomere HPA provides a convenient and useful tool for the examination of G-tail length with a high-throughput platform using genomic DNA or cell lysate. G-tail telomere HPA may be applicable for clinical diagnostics as well as drug target screening.

Key words: G-tail, Hybridization protection assay, High-throughput, Risk assessment, Cancer, Aging

1. Introduction

Mammalian telomeric DNA consists of 5′-(TTAGGG)$_n$-3′ double-stranded repeats, followed by up to several hundred bases of G-rich single-stranded 3′-overhang, the so-called telomere G-tail (1, 2). Telomeres are gradually shortened with cell division due to problems with end replication (3, 4). Telomere repeat sequences are synthesized by the telomerase, a cellular ribonucleoprotein reverse transcriptase (5). Expression of the catalytic subunit of the human telomerase gene, hTERT, correlates with the presence of telomerase activity in human cells (6), and introduction of the hTERT gene alone into normal cells is sufficient to induce telomerase activity, followed by telomere elongation and cell immortalization (7, 8). The single-stranded telomere G-tail is a key structure that protects telomere DNA from DNA damage and chromosome instability. The G-tail invades into double-stranded telomere DNA, leading to the formation of the so-called

Zhou Songyang (ed.), *Telomeres and Telomerase: Methods and Protocols*, Methods in Molecular Biology, vol. 735,
DOI 10.1007/978-1-61779-092-8_6,

t-loop. G-tail length is essential for chromosome capping (9). In addition, shelterin proteins TRF1, TRF2, POT1, TPP1, TIN2, and Rap1 also required for t-loop formation (9). Knockdown of these genes can affect G-tail length alterations and chromosome stability (10, 11). For example, when either TRF2 or POT1 is inhibited by dominant negative forms of the proteins, the overall amount of G-tail is diminished (12, 13). In the case of TRF2 inhibition, ERCC1/XPF-deficient cells retained the G-tail after TRF2 inhibition, suggesting that the loss of G-tail might involve ERCC1/XPF NER endonuclease which can remove 3′-overhang DNA (14). Taken together, G-tail alterations may be a good indicator for stability of the t-loop structure that protects chromosome ends.

Hybridization protection assay (HPA) utilizes probes that are labeled with a nonradioactive chemiluminescence compound – acridinium ester (AE) detector molecule that emits a chemiluminescent signal, and has been used for the detection of total telomere length and telomerase activity (15, 16). HPA reaction does not require physical separation of unhybridized vs. hybridized probe, therefore, HPA-based assays including G-tail telomere HPA can be applicable for high-throughput screening.

2. Materials

1. Hybridization buffer: 0.1 M succinic acid, 0.23 M lithium hydroxide monohydrate, 2% lithium lauryl sulfate, 1.2 M lithium chloride, 20 mM EDTA·2Na, 20 mM EGTA, 15 mM 2,20-dithiodipyridine, adjusted to pH 4.7 with HCl.
2. Hydrolysis buffer: 0.6 M boric acid, 182 mM NaOH, 1% Triton X-100, adjusted to pH 8.5 with NaOH.
3. Synthesized human telomere oligonucleotide: an 84mer of 5′-$(TTAGGG)_{14}$-3′ or a 35mer of 5′-$(TTAGGG)_6$-TTAGG-3′.
4. Acridinium ester (AE)-labeled telomere probe: 5′-CCCTAA CCCTAACC*CTAACCCTAACCCTA-3′ [*AE position, 8×10^7 rlu/pmol probe DNA made by Fujirebio, Inc., (Tokyo, Japan)].
5. GEN-PROBE detection reagent kit: Catalog No. 1791, Kit contains Detection Reagent I (0.1% hydrogen peroxide in 0.001 N nitric acid) and Detection Reagent II (1 N sodium hydroxide).
6. Spectrophotometer such as NanoDrop (Thermo scientific).
7. Luminometer (Leader I, Gen-Probe, Inc., San Diego, CA).

3. Methods

3.1. Preparation of Genomic DNA for G-Tail Telomere HPA

1. Purify genomic DNA from cultured cells or clinical samples including tissues and blood using a phenol–chloroform-based method (see Note 1).
2. Store genomic DNA at 4°C or −20°C until use, or proceed directly to step 3.
3. Shear genomic DNA using a 24 G syringe at least ten times. Be sure to confirm that DNA solution is homogenous. This step does not have an effect on G-tail length or total telomere length.
4. Centrifuge at 8,000×*g* for 5 min.
5. Collect the supernatant and transfer to new tube.
6. Measure DNA concentration by NanoDrop.
7. Store at −20°C until ready to use.

3.2. Preparation of Diluted Telomere Oligonucleotide and Diluted Genomic DNA Samples for G-tail Telomere HPA

1. Make a series of dilutions of the synthesized human telomere oligonucleotide for making a standard curve of the assay: 1.0, 0.5, 0.1, 0.05, 0.01, and 0.005 nM (see Note 2).
2. Transfer 10 μL of each dilution of the oligonucleotide into a 5 mL polypropylene tube and add 90 μL of sterilized water. Make a duplicate for each dilution, and a pair of blanks without oligonucleotide. Proceed to Subheading 3.3, step 1, after preparation of diluted genomic DNA.
3. For the detection of telomere G-tails in genomic DNA, 5 μg of non-denatured human genomic DNA is typically used for each assay. Dilute purified genomic DNA with TE buffer to 5 μg/100 μL. Prepare 400 μL of diluted genomic DNA, if both G-tail and total telomere length are measured (see Note 3).

3.3. G-Tail Measurement by G-Tail Telomere HPA (Fig. 1)

1. Transfer 100 μL of each diluted genomic DNA sample (Preheat at 50°C is recommended) to a Falcon BD 352053 tube.
2. Transfer 100 μL (containing 5 μg) of the non-denatured genomic DNA to 5 mL polypropylene tubes. Make a triplicate for each sample.
3. Denature 80 μL of remaining genomic DNA at 99°C for 10 min, and then immediately transfer to iced water and cool for 2 min.
4. For the detection of double-stranded telomere regions with G-tails (total telomere) in genomic DNA, 1 μg denatured human genomic DNA is typically used. Transfer 20 μL (containing 1 μg) of the genomic DNA to a 5 mL polypropylene tube, and add 80 μL of sterilized water. Make a triplicate for each sample.

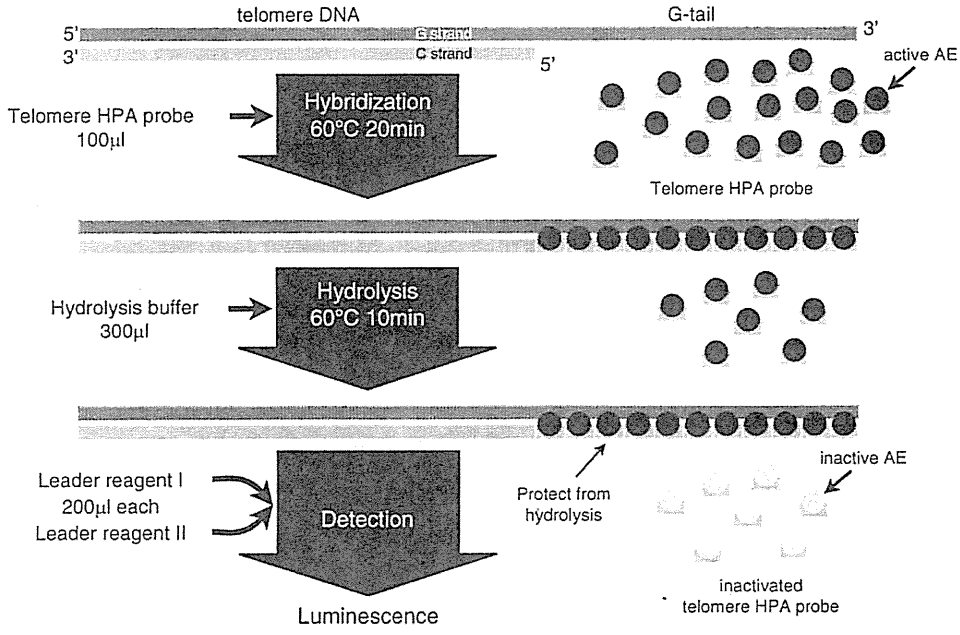

Fig. 1. The principle of G-tail telomere HPA. G-tail telomere HPA consists of three steps: "hybridization," "Hydrolysis," and "Detection" for the measurement of relative G-tail length from purified genomic DNA as well as nonpurified cell lysate using single tube. First step, "hybridization step": incubation of non-denatured genomic DNA with acridinium ester-labeled telomere HPA probe at 60°C for 20 min. Second step, "Hydrolysis step": incubation of reaction solution at 60°C for 10 min after adding hydrolysis buffer to inactivate unhybridized telomere HPA probe. Hybridized telomere HPA probe can be protected the inactivation of acridinium ester from hydrolysis. Last step, "Detection step": detection of luminescence from hybridized probe after adding Detection buffer I and Detection buffer II using autoinjector-equipped luminometer.

5. Dilute AE-labeled telomere HPA probe to 3×10^5 rlu (relative light units)/mL.
6. Add 100 μL of diluted telomere HPA probe to the bottom of each tube for detecting standard telomere oligo, G-tails, and total telomere (final 3×10^5 rlu/assay). Vortex at maximum speed for 5 s.
7. Incubate all the tubes simultaneously in a 60°C water bath for 20 min without agitation. Cover top of tubes with aluminum foil and protect from light (see Note 4).
8. Remove all tubes to room temperature from the water bath and let them sit for 10 min.
9. Add 100 μL of hydrolysis buffer. Vortex at maximum speed for 5 s (see Note 5).
10. Incubate all the tubes simultaneously in the 60°C water bath for 10 min.
11. Transfer all tubes to ice cold water and leave for over 1 min.

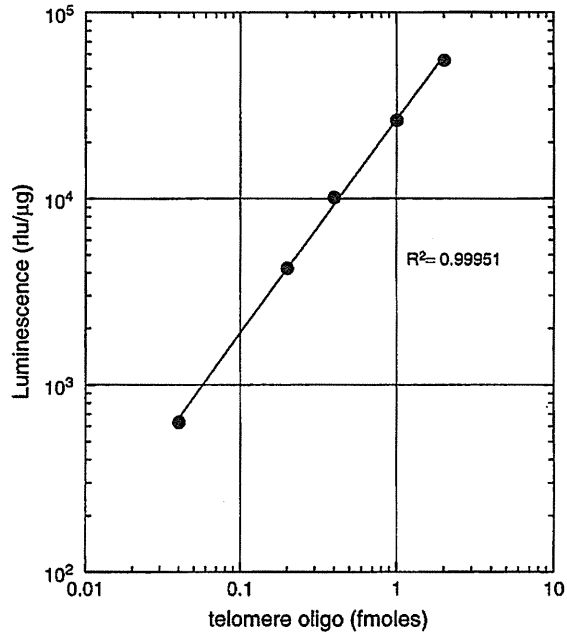

Fig. 2. The typical data of standard curve of G-tail telomere HPA using telomere oligonucleotide.

12. Measure chemiluminescence after injection of Detection Reagent I and Detection Reagent II using the autoinjector for 2 s per tube with a luminometer (see Note 6).
13. Luminescence value, RLU (relative luminescence unit), should be normalized to actual genomic DNA concentration as measured in Subheading 3.1, step 6.
14. Typical results of standard curves using telomere oligonucleotides are shown in Fig. 2. R2 is typically nearly 0.9999.
15. Typical results of the G-tail assay using genomic DNA are shown in Fig. 3. The luminescence signal (RLU) was normalized with the amount of genomic DNA in the tubes.

4. Notes

1. Do not use any genomic purification kits that utilize filters or beads.
2. Diluted oligonucleotide cannot be reused even if stored at -20°C or -80°C. Make fresh every time.

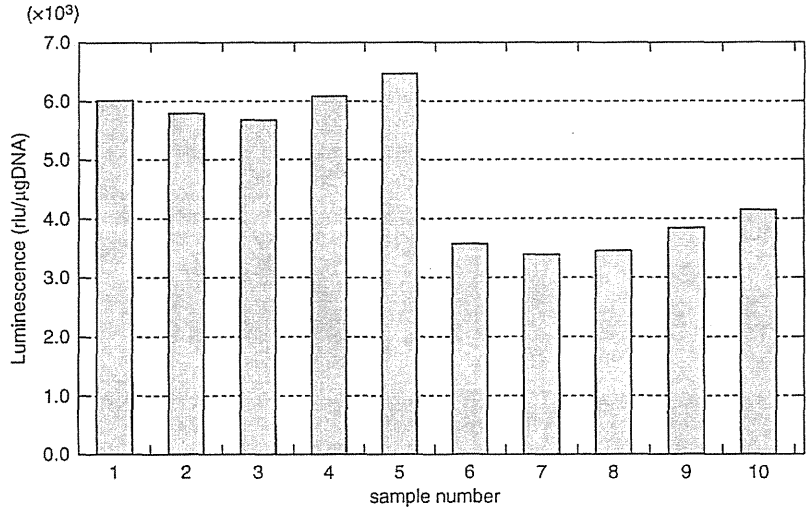

Fig. 3. The typical data of relative G-tail signals of human genomic DNA samples isolated from different persons using G-tail telomere HPA.

3. To normalize by the amount of genomic DNA, take 2 μL of DNA solution before starting following step. This step eliminate to measure DNA exact amount in each tube.
4. Do not use a heat block without water for this incubation step.
5. Make sure all reaction solution should be mixed with hydrolysis buffer, residual solution may cause nonspecific signals due to insufficient inactivation of unhybridized probe.
6. An autoinjector is essential for this assay. Luminescence should be counted from 0 to 2 s. Follow the instruction manual of the equipment.

References

1. Makarov, V. L., Hirose, Y., and Langmore, J. P. (1997) Long G tails at both ends of human chromosomes suggest a C strand degradation mechanism for telomere shortening, *Cell* 88, 657–666.
2. Wright, W. E., Tesmer, V. M., Huffman, K. E., Levene, S. D., and Shay, J. W. (1997) Normal human chromosomes have long G-rich telomeric overhangs at one end, *Genes Dev* 11, 2801–2809.
3. Olovnikov, A. M. (1971) [Principle of marginotomy in template synthesis of polynucleotides], *Dokl Akad Nauk SSSR* 201, 1496–1499.
4. Watson, J. D. (1972) Origin of concatemeric T7 DNA, *Nat New Biol* 239, 197–201.
5. Greider, C. W., and Blackburn, E. H. (1985) Identification of a specific telomere terminal transferase activity in Tetrahymena extracts, *Cell* 43, 405–413.
6. Nakamura, T. M., Morin, G. B., Chapman, K. B., Weinrich, S. L., Andrews, W. H., Lingner, J., Harley, C. B., and Cech, T. R. (1997) Telomerase catalytic subunit homologs from fission yeast and human, *Science* 277, 955–959.
7. Nakayama, J., Tahara, H., Tahara, E., Saito, M., Ito, K., Nakamura, H., Nakanishi, T., Ide, T., and Ishikawa, F. (1998) Telomerase

activation by hTRT in human normal fibroblasts and hepatocellular carcinomas, *Nat Genet* **18**, 65–68.

8. Bodnar, A. G., Ouellette, M., Frolkis, M., Holt, S. E., Chiu, C. P., Morin, G. B., Harley, C. B., Shay, J. W., Lichtsteiner, S., and Wright, W. E. (1998) Extension of life-span by introduction of telomerase into normal human cells, *Science* **279**, 349–352.
9. de Lange, T. (2004) T-loops and the origin of telomeres, *Nat Rev Mol Cell Biol* **5**, 323–329.
10. de Lange, T. (2005) Shelterin: the protein complex that shapes and safeguards human telomeres, *Genes Dev* **19**, 2100–2110.
11. Palm, W., and de Lange, T. (2008) How shelterin protects mammalian telomeres, *Annu Rev Genet* **42**, 301–334.
12. Hockemeyer, D., Sfeir, A. J., Shay, J. W., Wright, W. E., and de Lange, T. (2005) POT1 protects telomeres from a transient DNA damage response and determines how human chromosomes end, *EMBO J* **24**, 2667–2678.
13. van Steensel, B., Smogorzewska, A., and de Lange, T. (1998) TRF2 protects human telomeres from end-to-end fusions, *Cell* **92**, 401–413.
14. Zhu, X. D., Niedernhofer, L., Kuster, B., Mann, M., Hoeijmakers, J. H., and de Lange, T. (2003) ERCC1/XPF removes the 3' overhang from uncapped telomeres and represses formation of telomeric DNA-containing double minute chromosomes, *Mol Cell* **12**, 1489–1498.
15. Hirose, M., Abe-Hashimoto, J., Ogura, K., Tahara, H., Ide, T., and Yoshimura, T. (1997) A rapid, useful and quantitative method to measure telomerase activity by hybridization protection assay connected with a telomeric repeat amplification protocol, *J Cancer Res Clin Oncol* **123**, 337–344.
16. Nakamura, Y., Hirose, M., Matsuo, H., Tsuyama, N., Kamisango, K., and Ide, T. (1999) Simple, rapid, quantitative, and sensitive detection of telomere repeats in cell lysate by a hybridization protection assay, *Clin Chem* **45**, 1718–1724.

Published April 18, 2011

miR-22 represses cancer progression by inducing cellular senescence

Dan Xu,[1] Fumitaka Takeshita,[3] Yumiko Hino,[1] Saori Fukunaga,[1] Yasusei Kudo,[2] Aya Tamaki,[1] Junko Matsunaga,[1] Ryou-u Takahashi,[3] Takashi Takata,[2] Akira Shimamoto,[1] Takahiro Ochiya,[3] and Hidetoshi Tahara[1]

[1]Department of Cellular and Molecular Biology and [2]Department of Oral Maxillofacial Pathobiology, Graduate School of Biomedical Science, Hiroshima University, Minami-ku, Hiroshima 734-8553, Japan
[3]Division of Molecular and Cellular Medicine, National Cancer Center Research Institute, Chuo-ku, Tokyo 104-0045, Japan

Cellular senescence acts as a barrier to cancer progression, and microRNAs (miRNAs) are thought to be potential senescence regulators. However, whether senescence-associated miRNAs (SA-miRNAs) contribute to tumor suppression remains unknown. Here, we report that miR-22, a novel SA-miRNA, has an impact on tumorigenesis. miR-22 is up-regulated in human senescent fibroblasts and epithelial cells but down-regulated in various cancer cell lines. miR-22 overexpression induces growth suppression and acquisition of a senescent phenotype in human normal and cancer cells. miR-22 knockdown in presenescent fibroblasts decreased cell size, and cells became more compact. miR-22–induced senescence also decreases cell motility and inhibits cell invasion in vitro. Synthetic miR-22 delivery suppresses tumor growth and metastasis in vivo by inducing cellular senescence in a mouse model of breast carcinoma. We confirmed that CDK6, SIRT1, and Sp1, genes involved in the senescence program, are direct targets of miR-22. Our study provides the first evidence that miR-22 restores the cellular senescence program in cancer cells and acts as a tumor suppressor.

Introduction

Tumor progression is a multistep process wherein several defined events are common to cancer cells, such as uncontrolled proliferation and invasion (Hahn and Weinberg, 2002). Cellular senescence is characterized by an irreversible arrest of cell proliferation, so that it can prevent the aberrant and unlimited proliferation of tumor cells (Campisi, 2005). Senescent cells exhibit enlarged morphological changes and less motility than young cells, which may contribute to the suppression of cell migration, invasion, and metastasis (Chen et al., 2000). Oncogene-induced senescence is a cellular response, which can occur in vivo and provides a bona fide barrier to tumorigenesis (Narita and Lowe, 2005). Oncogene-induced senescence was found in premalignant tumors but not in more advanced malignant tumors (Braig et al., 2005; Collado et al., 2005). Therefore, cellular senescence acts as an important barrier to cancer and plays an important role in tumor suppression.

Correspondence to Hidetoshi Tahara: toshi@hiroshima-u.ac.jp

Abbreviations used in this paper: cont miR, control miRNA; HPA, hybridization protection assay; hTERT, human telomerase reverse transcriptase; LNA, locked nucleic acid; miRNA, microRNA; PDL, population doubling level; pRb, retinoblastoma protein; SA-β-gal, senescence-associated β-galactosidase; SAHF, senescence-associated heterochromatin foci; SA-miRNA, senescence-associated miRNA; UTR, untranslated region; WT, wild type.

microRNAs (miRNAs) are a class of naturally occurring small noncoding RNAs that negatively regulate the stability and translation of target protein–coding mRNAs at the 3′ untranslated region (UTR). miRNAs typically target a cluster of genes rather than one specific gene (Bartel, 2004), a characteristic which allows them to play critical roles in a variety of biological processes such as cell proliferation, differentiation, apoptosis, and carcinogenesis (He and Hannon, 2004). Recently, a growing number of studies have documented the miRNA expression profiles in human cancers (Calin and Croce, 2006), suggesting that miRNAs emerge as novel biomarkers for various cancers. However, there is currently little information about miRNA profiling studies and biological effects of miRNAs in cellular senescence.

The senescence program is established and maintained by p53 and retinoblastoma protein (pRb) tumor suppressor pathways. The requirements of p53 and pRb for the induction of cellular senescence vary in their prominence depending on the genetic context, species, and cell type (Adams, 2007; Schmitt, 2007;

Supplemental Material can be found at:
http://jcb.rupress.org/content/suppl/2011/04/18/jcb.201010100.DC1.html
Original image data can be found at:
http://jcb-dataviewer.rupress.org/jcb/browse/4262

The Rockefeller University Press $30.00
J. Cell Biol. Vol. 193 No. 2 409–424
www.jcb.org/cgi/doi/10.1083/jcb.201010100

Published April 18, 2011

Haferkamp et al., 2009). Recently, various studies have indicated that some miRNAs, such as miR-34a and miR-20a, induce senescence-like growth arrest through regulating cell cycle genes and senescence-associated genes involved in the p53 and/or pRb pathway (Tazawa et al., 2007; Poliseno et al., 2008; Sun et al., 2008). Such miRNAs play a direct role in senescence and are called senescence-associated miRNAs (SA-miRNAs; Lafferty-Whyte et al., 2009).

In the present study, we attempted to screen SA-miRNAs that control cellular senescence in human fibroblasts, and we report here that miR-22 is a novel SA-miRNA that functions in mediating cellular senescence. We studied the role of miR-22 in cellular senescence using human normal cells and cancer cell lines as an in vitro culture system as well as an in vivo mouse breast tumor model. Upon senescence, cells become flattened and enlarged and exhibit biochemical changes such as the increased perinuclear activity of senescence-associated β-galactosidase (SA-β-gal; Dimri et al., 1995; Narita et al., 2003). Another critical event during the cellular senescence process is a decrease in cell growth and cell motility. We found a widespread decrease of miR-22 expression in various human cancer cell lines. Introduction of miR-22 into cancer cells inhibits cell proliferation, accompanied by senescence-like cell morphology and a decrease in cell motility and invasiveness. We predicted the putative direct targets of miR-22 by the computational prediction of targets based on sequence match to the miRNA. We identified three targets, including CDK6, Sp1, and SIRT1, which are directly regulated by miR-22. Furthermore, silencing of these targets resulted in growth arrest and increased SA-β-gal activity, accompanied by pRB dephosphorylation. We confirmed that miR-22 regulated the pRb pathway of cellular senescence through targeting of CDK6 and SIRT1. Ectopic expression of CDK6, SIRT1, or Sp1 could partially rescue the senescence phenotypes in miR-22–transfected cells. Significantly, miR-22 injection suppresses tumor growth and metastasis in vivo by induction of senescence in breast tumor, suggesting that SA-miRNA miR-22 acts as an important barrier to cancer and plays an important role in tumor suppression. Our findings provide new insight for the role of SA-miRNAs between cellular senescence and tumorigenesis.

Results

miR-22 overexpression induces cellular senescence in human fibroblasts

To identify miRNAs that control cellular senescence, we analyzed miRNA expression profiling by miRCURY locked nucleic acid (LNA) miRNA array in young and senescent TIG-3 fibroblasts (Fig. 1 A). We found that a set of altered expression miRNAs has been reported to be involved in cell growth and tumorigenesis (Fig. 1 A and Table S1). Among them, the majority of antigrowth miRNAs were expressed two– to fourfold more in senescent TIG-3 cells than in young cells. To confirm and validate the results, we performed 3D-Gene miRNA microarray to evaluate miRNA expression levels. Two kinds of microarray analysis showed that five miRNAs are uniformly up-regulated by twofold or greater in senescent compared with young cells. These include miR-22, miR-34a, miR-125a-5p, miR-24-2*, and miR-152, several of which, namely miR-34a and miR-125a-5p, are closely associated with senescence-like growth arrest and metastasis in cancer cells (Tazawa et al., 2007; Li et al., 2009; Wang et al., 2009). Here, we focused on miR-22 and evaluated the expression of miR-22 in young and senescent human diploid fibroblast strains. Quantitative (q) RT-PCR analysis confirmed that miR-22 expression was increased in senescent TIG-3 and other fibroblasts and even up-regulated by more than fivefold in senescent MRC-5 cells (Fig. 1 B). These findings suggest that miR-22 up-regulation is universal in senescent human fibroblasts.

To investigate the involvement of miR-22 in cellular senescence in human fibroblasts, we enforced miR-22 expression by introduction of mature miR-22 duplex into young fibroblasts. We first examined miR-22 expression level by qRT-PCR analysis at day 6 after direct transfection with miR-22 duplex into young MRC-5 cells (Fig. 1 C). Compared with the endogenous level of miR-22 in the senescent MRC-5 cells (fivefold higher than young cells), miR-22 was up-regulated by 2.9-fold (1 nM), 4-fold (5 nM), and 15.7-fold (10 nM) in MRC-5 cells, relative to control miRNA (cont miR) in each transfection group. Furthermore, miR-22 also increased SA-β-gal activity (Fig. 1 D), a well known senescence cytosolic biomarker, in a transfection dose-dependent manner, whereas cont miR did not induce SA-β-gal activity. These results imply that up-regulation of miR-22 expression is significant for the induction of senescence phenotypes. Because the cessation of cell proliferation is a hallmark of cellular senescence, we examined whether cell proliferation is altered by overexpression of miR-22. We observed that transfection of 10 nM miR-22 caused a remarkable inhibition of cell proliferation compared with that of cont miR (Fig. 1 E), and this growth inhibition by miR-22 is in a dose-dependent manner (not depicted). Senescence-associated heterochromatin foci (SAHF) formation is thought to be a senescence nuclei biomarker and is often observed in senescent fibroblasts (Dimri et al., 1995; Narita et al., 2003; Adams, 2007). We observed obvious SAHF formation in miR-22–transfected cells, and the percentage of SAHF-positive cells was significantly increased by miR-22 overexpression and was also increased in senescent MRC-5 cells (Fig. 1 F). This result is not cell type specific because other fibroblasts, such as IMR90, transfected with miR-22 appeared to be senescence phenotypes (unpublished data).

To ensure that the function of mature miRNA is not at a supraphysiological level, we repeated these experiments using a stable miRNA vector that mimics miRNA biological processing. Pre–miR-22 lentiviral construct (Lenti-Pre22), stably expressing miR-22 precursor in its native context, was used to study the effect of miR-22 on cellular senescence in MRC-5 fibroblasts. Lenti-Pre22–infected cells exhibited the enlarged senescence morphology and SA-β-gal–positive staining (Fig. 2 A). Compared with Lentiviral empty vector (Lenti-C), Lenti-Pre22 infection significantly increased SA-β-gal activity and caused growth arrest in MRC-5 cells (Fig. 2, A and B), which is similar to the effect of mature miR-22. Collectively, these results suggest that miR-22 is associated with cellular senescence, accompanied by the induction of major specific senescence-associated markers in human diploid fibroblasts.

Published April 18, 2011

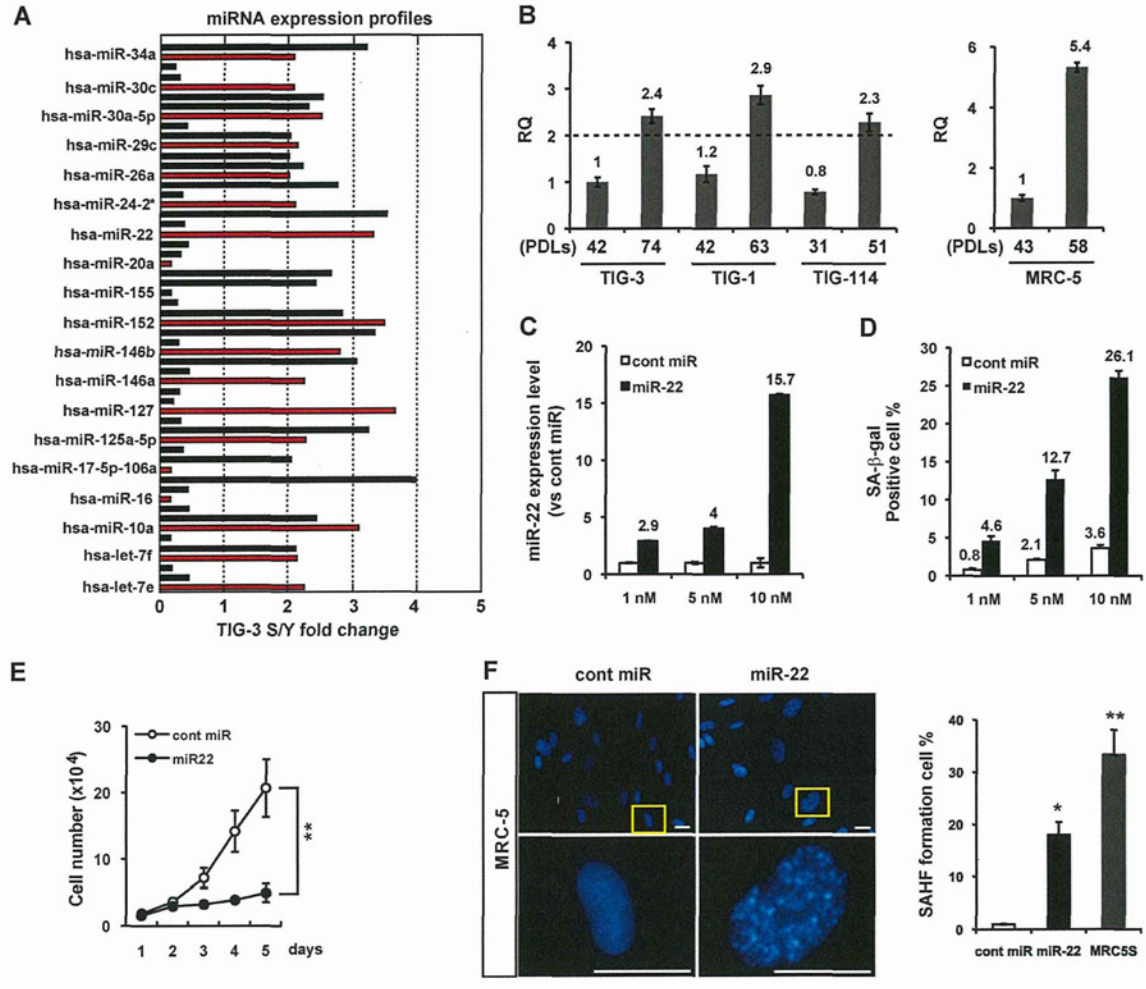

Figure 1. **miR-22 is up-regulated in senescent human fibroblasts, mediating cellular senescence.** (A) miRNA expression profile of TIG-3 fibroblasts was analyzed by miRNA microarray, presented as fold changes in miRNA expression between TIG-3S (senescent) and young (Y) cells. A set of altered expression miRNAs is indicated by red columns (see Table S1). RQ, relative quantitation. (B) Relative quantitation of miR-22 expression in different PDLs of fibroblasts was analyzed by qRT-PCR analysis. miR-22 expression levels in human fibroblasts were indicated, relative to those in TIG-3 (42 PDL) set at 1 in the left histogram and MRC-5 (43 PDL) set at 1 in the right histogram. U6 was used as an internal normalization control. The dashed line represents the threshold of expression level (twofold vs. TIG-3 42 PDL). (C and D) MRC-5 cells were transfected with cont miR or mature miR-22 (miR-22) for 6 d at indicated concentration. (C) qRT-PCR analysis shows the relative quantitation of miR-22 expression (vs. cont miR) in each transfection group. miR-22 expression levels in miR-22–transfected MRC-5 cells were indicated, relative to that in cont miR–transfected cells set at 1. U6 was used as an internal normalization control. (D) SA-β-gal activity was presented by the percentage of SA-β-gal–positive cells, which was indicated in different dose groups. (E) Cell proliferation assay was performed after transfection of 10 nM miR-22 or cont miR, and cells were counted for the indicated days. Each value was determined in triplicate. **, $P < 0.01$. (F) Representative photos for SAHF formation in MRC-5 cells at day 6 after transfection. Images were taken with fluorescence microscopy. Enlarged images of the boxed area from the top are shown in the bottom. SAHF formation was quantified by counting 200 cells from >10 random fields, and the results were shown in the right histogram in contrast to MRC5S (senescent; 58 PDL). Data in all the panels represent mean ± SEM ($n = 3$). *, $P < 0.05$; **, $P < 0.01$. Bars, 20 µm.

Furthermore, we wondered how knockdown of miR-22 impacts cellular senescence phenotypes and whether a reduced expression of miR-22 would impede the progression of senescence and extend the life span in fibroblasts. miRZip anti–miR-22 expression lentivector (anti-22), which can stably express anti–miR-22 and provide permanent miR-22 inhibition, was used to infect young (44 population doubling level [PDL]) and presenescent (54 PDL) MRC-5 cells. We observed that Leni-Pre22–infected young MRC-5 cells demonstrated enlarged senescent morphological changes (Fig. 2 C, GFP-labeled cells marked with yellow arrowheads). In contrast, anti-22–infected young MRC-5 cells seemed smaller and younger than anti-22 empty vector (anti-C)–treated cells (Fig. 2 D). For presenescent MRC-5 cells, stable knockdown of miR-22 caused obvious morphological changes, exhibiting small and thin morphology (Fig. 2 C, GFP-labeled cells marked with arrows), whereas those cells that failed to be infected exhibited enlarged senescent morphology (Fig. 2 C, white triangles) within the same field under the fluorescent microscope. Presenescent MRC-5 cells entered senescence and demonstrated obvious SA-β-gal staining as time passed. Anti-22–infected presenescent MRC-5 cells maintained small and thin morphology for >2 wk with a decreased percentage of SA-β-gal–positive cells (Fig. 2 E), and there appeared to be a significant decrease in cell size and percentage of cells

Published April 18, 2011

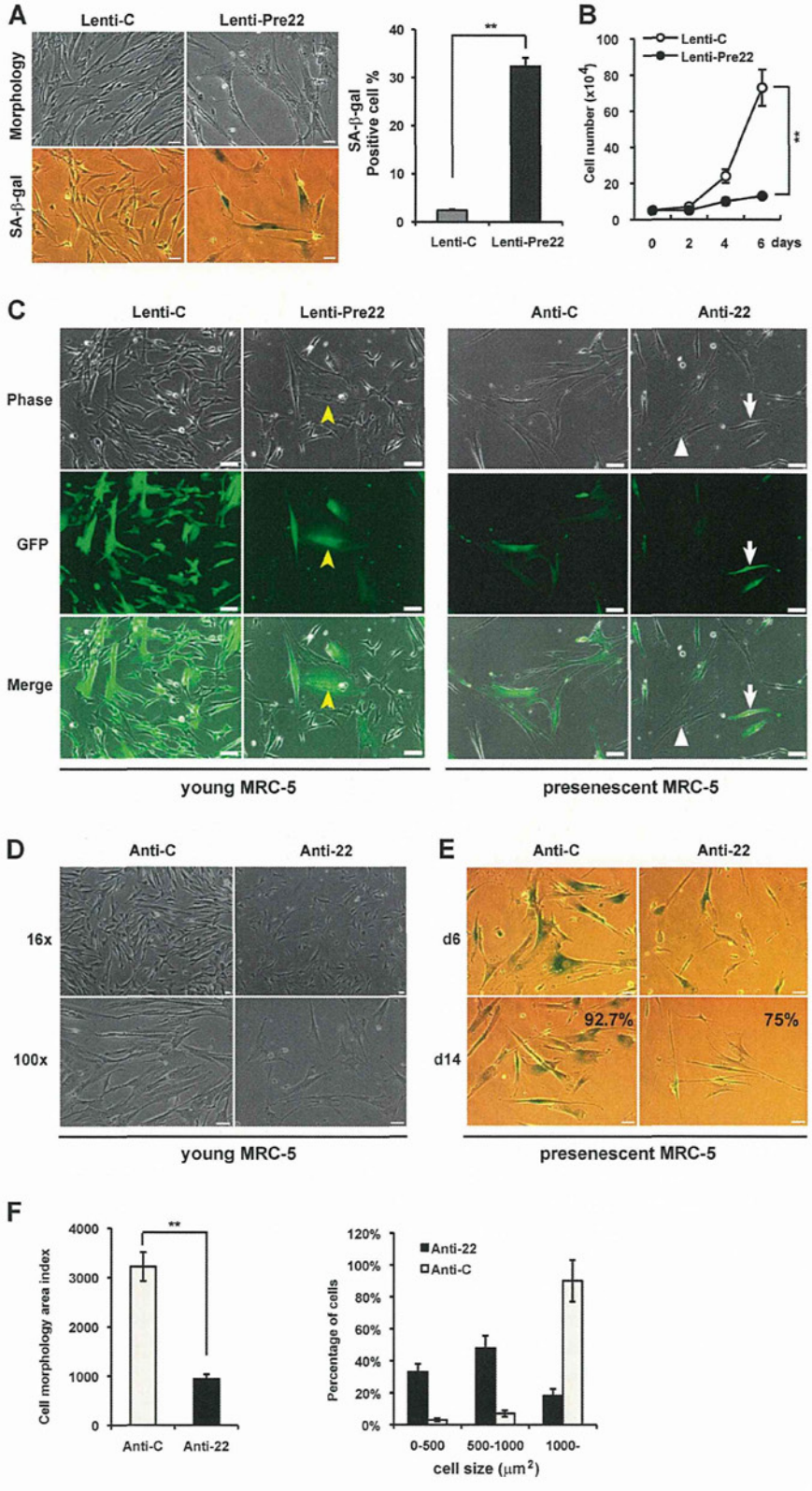

Figure 2. **Stable expression and knockdown of miR-22 affect senescence phenotypes in MRC-5 cells.** (A) Cell morphology and SA-β-gal activity were analyzed by phase-contrast microscopy at day 6 after infection with empty vector (Lenti-C) or premiR-22 (Lenti-Pre22). The percentage of SA-β-gal–positive cells is presented in the right histogram. (B) Cell proliferation assay was performed after infection of Lenti-Pre22, and cells were counted for the indicated days, compared with control cells. Each value was determined in triplicate. **, $P < 0.01$. (C) Cell morphology was analyzed with fluorescence microscopy at day 6 after infection. GFP-labeled cells indicate infected cells (middle). Yellow arrowheads and white arrows depict miR-22 overexpression in young MRC-5 cells and miR-22 knockdown in presenescent MRC-5 cells, respectively. Those cells that failed to be infected are marked with white triangles. (D) Cell morphology of anti-22–infected young MRC-5 was analyzed by phase-contrast microscopy and compared with anti-C. (E) Presenescent MRC-5 cells infected with anti-C or anti-22 were subjected to SA-β-gal assay at days 6 and 14 after infection. The percentage of SA-β-gal–positive cells at day 14 after infection is presented in the bottom panels. (F) Cell morphology area and cell size distribution were analyzed using ImageJ by counting GFP-expressed presenescent MRC-5 cells after infection with anti-C or anti-22 for 6 d. Cell morphology area index represents cell size (micrometers squared). Cell size distribution was divided into three groups: 0–500, 500–1,000, and 1,000 μm^2 and up. Data in all the panels represent mean ± SEM ($n = 3$). **, $P < 0.01$. Bars: (A, D, and E) 50 μm; (C) 20 μm.

distributed in a large-sized group (Fig. 2 F), compared with senescent anti-C–treated cells. Although stable knockdown of miR-22 exhibited neither the promotion of cell proliferation nor the extension of the life span (not depicted), this might be a result of irreversible growth arrest in senescent cells. These findings suggest the requirement of miR-22 in mediating senescence and indicate that miR-22 inhibition is indeed an obstacle for the progression of senescence in fibroblasts.

Published April 18, 2011

miR-22 overexpression induces growth suppression and senescence-like phenotypes in human breast epithelial and cancer cells

Senescence has been most widely studied in fibroblasts in vitro but is also well defined in other cell types, such as epithelial cells which are the origin of most carcinoma (Narita et al., 2003). Expression of human telomerase reverse transcriptase (hTERT) in certain cell types has been shown to extend cellular life span without malignant transformation. To investigate the effect of miR-22 on cellular senescence in human epithelial cells, we used hTERT-infected HMEC184 (184hTERT) cells that possess the unlimited proliferation capacity of HMEC184 cells and are regarded as immortalized. We found that miR-22 was expressed higher by >2.5-fold in senescent HMEC184 (22 PDL) than in 184hTERT cells that have a similar miR-22 expression level to that of normal young HMEC184 (Fig. 3 A). Compared with immortalized 184hTERT cells, a widespread decrease in miR-22 level was observed in various human cancer cells (Fig. 3 A), indicating that miR-22 may have an intrinsic function in tumor suppression associated with various human malignancies.

To test this notion, we first evaluated the effect of miR-22 on cell growth and SA-β-gal activity in human breast epithelial cells and two breast cancer cell lines. We found that miR-22 significantly inhibited cell growth in 184hTERT, MCF7, and MDA-MB-231-luc-D3H2LN (called MDA-D3 for short; Fig. 3 B). We noted that mature miR-22 caused remarkable and characteristic morphological alterations, including enlarged cellular size and a flattened shape (Fig. 3 C), and significantly increased SA-β-gal activity in the three cells (Fig. 3 D). Furthermore, we confirmed that overexpression of premiR-22 in MDA-D3 cells also significantly induced senescence-specific morphological changes, increased SA-β-gal activity (Fig. 3 E), and inhibited cell growth (Fig. 3 F), similar to the effect of mature miR-22.

The marked induction of senescence by miR-22 in human breast cancer cells prompted us to investigate whether miR-22 induces cellular senescence in other human cancer cells. Therefore, we further studied the effect of miR-22 in the human cervical carcinoma cell line SiHa. We confirmed the dose-dependent increase in miR-22 expression level (Fig. 4 A) and SA-β-gal activity (Fig. 4 B) after direct transfection of miR-22 in SiHa cells, whereas cont miR affected neither the cell growth nor the SA-β-gal activity. Introduction of 10 nM miR-22 resulted in cells exhibiting a senescence-like flattened shape and SA-β-gal–positive staining (Fig. 4 C), and it induced remarkable growth suppression compared with that of cont miR (Fig. 4 D). Because senescent cells never reenter the cell cycle and appear to decrease in DNA synthesis, we performed FACS analysis and quantity analysis of BrdU incorporation in SiHa cells. miR-22 overexpression induced cell cycle arrest at G1 phase, accompanied by the decrease in percentages of S phase (Fig. 4 E). The inhibitory effect of miR-22 on cell cycle progression has also been recently reported in other cancer cells (Ting et al., 2010). Furthermore, miR-22 resulted in the decrease of BrdU incorporation in comparison with cont miR or miR-34a (Fig. 4 F), indicating impaired DNA replication in miR-22–transfected cells during the S phase of the cell cycle. In addition, we confirmed that miR-22 expression was increased in Lenti-Pre22–infected SiHa cells (Fig. 4 G) close to the expression level of miR-22 (10 nM). Lenti-Pre22 also induced senescence-specific morphological changes, increased SA-β-gal activity, and inhibited cell growth (Fig. 4, H and I), indicating the induction of cellular senescence by miR-22 overexpression in SiHa cells.

Moreover, we did not observe any significant increase in TUNEL-positive apoptotic cells in miR-22–transfected SiHa and MDA-D3 cells (Fig. S1, A and B). These findings suggest that the growth suppression induced by miR-22 overexpression was caused by the induction of G1 arrest in cellular senescence rather than apoptosis. In reverse, miR-22 knockdown in cancer cells resulted in various morphological changes and differential timing of apoptosis in different cell lines. Anti-22–infected SiHa cells appeared to be small and underwent apoptosis at day 6 after infection (Fig. S1 C), whereas MDA-D3 cells became rounded and apoptotic cells were observed in anti-22–infected cells from the third day after infection (Fig. S1 D), which might be because the timelines for the progression of different cells through apoptosis vary in different cell lines (Jessel et al., 2002).

Various findings have suggested the critical role of telomere shortening in contributing to cellular senescence in human cells (Deng et al., 2008). Telomeric 3′-overhang (G-tail) is essential for proper telomere function (Tahara et al., 2005). Here, overexpression of miR-22 had no effect on the length of either total telomere or G-tail (Fig. S2), indicating that miR-22–induced senescence is possibly independent of telomere shortening.

SIRT1, Sp1, and CDK6 are direct targets of miR-22

miRNAs are known to suppress hundreds of mRNA targets, resulting in global changes in the cellular phenotype of cells (He and Hannon, 2004). We therefore make an effort to identify potential targets for miR-22 using both in silico and experimental approaches. We used a consensus approach with three widely used types of software (miRanda, TargetScan, and PicTar) to perform the target prediction. After overlapping prediction analysis, we screened those genes that were down-regulated upon senescence and implicated in cell growth and cell cycle regulation. Based on this, SIRT1, Sp1, and CDK6 were selected to be putative miR-22 target genes. The mRNAs of SIRT1 and Sp1 contain putative binding sites for miR-22 in their 3′-UTRs, and each site is broadly conservative among mammals. CDK6 mRNA contains three miR-22 binding sites in the 3′-UTR, whereas it is different in conservation for each site (Fig. 5 A).

To address those genes directly regulated by miR-22, we performed luciferase reporter assay. We constructed pmirGLO full-length 3′-UTR of both SIRT1 and Sp1. Because the full-length 3′-UTR of CDK6 is too long (~10 kbp), human CDK6 3′-UTR containing three binding sites (6 kbp) was amplified and cloned into pmirGLO vector. Furthermore, to study which site in the 3′-UTR of each gene is important, we engineered luciferase reporters that have exact binding sites of 3′-UTRs of these genes including the wild type (WT) and two mutant UTRs (Mut1 and Mut2), as shown in Fig. 5 C. In SiHa and MDA-D3 cells, miR-22 significantly reduced the luciferase activities of the full-length 3′-UTR (Fig. 5 B) or WT SIRT1, SP1, and CDK6